IET Journals

The Institution of Engineering and Technology

Research Article

RPM and Doppler-based multi-path exploitation method for UWB TWR

Masafumi Setsu[1], Shouhei Kidera[1,2] ✉

[1]*Graduate School of Informatics and Engineering, The University of Electro-Communications, Tokyo 1828585, Japan*
[2]*Japan Society Science and Technology (JST), PRESTO, Saitama 3320012, Japan*
✉ *E-mail: kidera@uec.ac.jp*

Abstract: Through-the-wall radar (TWR) with ultra-wideband (UWB) signals is a promising technology for three-dimensional monitoring systems used for rescue and security applications. To develop a suitable imaging algorithm to deal with UWB radar data, the range points migration (RPM) method was enhanced for the TWR observation model. However, there are some problems in the actual application because multiple reflection signals from the walls or targets produce a ghost image. This research extends the RPM-based TWR imaging method to convert a ghost image to an accurate one by exploiting the double-bounced signals discriminated by the Doppler velocity. Such discrimination can be achieved by prior estimations for the motion and location of the target provided by the Doppler-associated RPM algorithm. The finite-difference time-domain-based numerical simulation, with the assumption of multiple surrounding walls, demonstrated that the authors proposed method produced an accurate object by converting a ghost image to an actual image.

1 Introduction

Through-the-wall radar (TWR) is a promising technology for various sensing applications such as the detection of human bodies buried under collapsed walls and furniture in rescue scenarios and the discovery of hostages or determination of the number of terrorists involved in crime scenes. Ultra-wideband (UWB) radar has several definitive advantages such as a high range resolution and sufficient penetration depth in the concrete wall. There are many studies that have investigated TWR imaging algorithms such as synthetic aperture radar [1], time-reversal approaches [2], wave equation inversion [3] or compressed sensing-based algorithms [4]. However, in the actual TWR scenario, the multipath scattering components among walls and targets should be considered, as this can produce ghost images, and there are some studies for suppression of ghost images [5, 6]. To address this problem, there have been intensive studies that have exploited multipath reflections to enhance spatial resolution and suppress ghost-image production [7, 8]. However, these methods are usually based on the assumption that a target constitutes an aggregation of point-wise targets, and these methods do not consider the motion of the scattering centre based on the sensor location. This motion causes inaccuracy in continuous boundary-shaped reconstruction such as for an ellipse. In addition, the conventional delay and sum (DAS) method require an expensive computation to obtain a full three-dimensional (3D) image, due to waveform-based integration in all possible regions.

A promising alternative approach, the range points migration (RPM) method, has been developed. Its effectiveness was validated using various observation models, where each observed RP (RP; a set of antenna locations and the measured range) is accurately converted to the corresponding scattered centre on the target boundary with a Gaussian-kernel-based direction-of-arrival (DOA) estimation. Several studies performed till date demonstrate the effectiveness of this method in terms of computational cost, accuracy and spatial resolution [9–11]. Furthermore, there are some extensions of RPM to the TWR imaging scenario [12], which are called TWR-based RPM (TW-RPM). However, the original TW-RPM suffers from ghost-image generation produced by multiple reflections between walls and objects.

A group led by Amin developed several promising studies that investigated multipath exploitation in TWR applications [13].

These studies examined how multipath reflection signals were focused by the DAS approach using prior knowledge of the wall arrangement. In this way, the energy of ghost images is effectively converted to the actual target location. Furthermore, compressive sensing (CS) multipath exploitation has been developed by the same group. CS multipath exploitation has the benefit of less data acquisition and enhanced resolution [14]. Other groups have developed an algorithm to determine the position of sidewalls via CS multipath exploitation [15], and an inverse scattering approach multipath exploitation to enhance the resolution [16]. Although the above methods are suitable for point-shaped scatter reconstruction, in the case of continuously shaped objects they could suffer from inaccuracy of shape reconstruction because the methods do not consider the physical basis that determines the scattering-centre location of the target as the scattering centre moves along the boundary according to the sensor location. As another approach for multiple-scattering exploitation, methods have been developed for dealing with shadow-region imaging for complex shapes or multiple targets without prior knowledge of the target shape, which is based on the DAS approach [17] or the RPM [18]. However, these algorithms require the strong assumption that either scattering centre of the double-bounced reflection should be reconstructed as an initial assumption, which is obtained by the single-scattering-based imaging method. This reconstruction requires a complicated process when dealing with a double-bounced signal.

The present study proposes a TW-RPM-based imaging method that incorporates double-bounced reflections, which are the most dominant reflections compared with other higher-order multipath reflections indicated by Doppler velocities. Using prior knowledge of the surrounding wall geometry (not target location or motion), the discrimination between direct- and double-bounced signals offers the potential to not only suppress a ghost image but to expand the reconstruction area of the target boundary. For the above discrimination, this paper introduces a Doppler–velocity-based discrimination that relies on the well-established assumption that direct- and double-bounced signals have different incident angles with different Doppler velocities. The above Doppler-based discrimination method is achieved through a priori estimation of the motion and location of the target, achieved by quantifying the temporal difference between the target boundary points sequentially reconstructed via the original TW-RPM. Note that, the
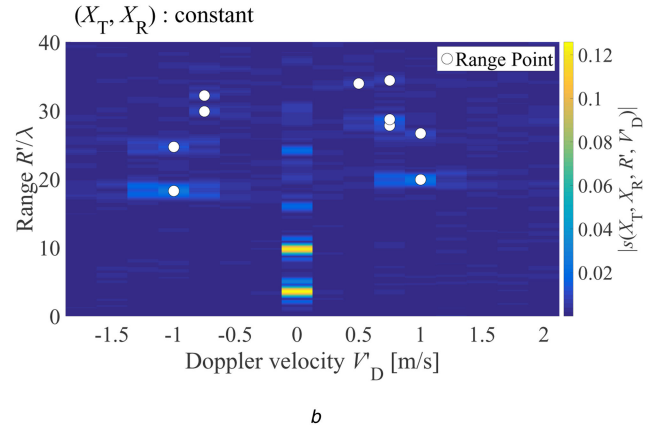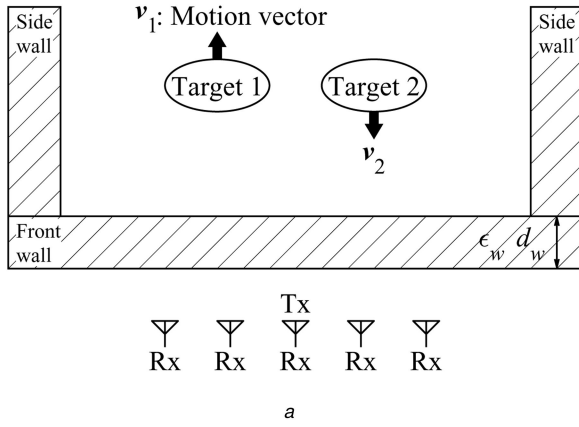
Fig. 1 *Observation model and RP extraction*
(a) Observation model, *(b)* Example of range–Doppler data and extracted RPs associated with Doppler velocity

proposed method does not only suppress the false image due to multiple scattering but also revive the multiple-scattering data to enhance the RPM imaging. In addition, the strong signal from a wall can be efficiently suppressed by eliminating zero–Doppler components. This method is also applicable to multiple objects by clustering the TW-RPM image in each snapshot and the grouping of different time images that have similar Doppler velocities. Furthermore, since reflection points corresponding to double-bounced and direct signals are generally located at different positions on the target boundary, the reconstructed area of the target boundary expands. This means that the apparent aperture size could be enhanced by this algorithm. The results of finite-difference time-domain (FDTD)-based numerical simulations demonstrated that our proposed method considerably suppressed ghost images and generated an accurate target boundary extraction for multipath TWR applications.

2 Observation model and RP extraction

Fig. 1*a* shows the observation model assumed for the typical TW imaging situation. It assumes that the kth target with an arbitrary boundary shape has a motion vector $\boldsymbol{v}_k$, which is a constant in the data acquisition sequence. Omni-directional antennas form linear array antennas in a straight line. For real-time tracking of targets and a simple hardware configuration, we assume single-input and multiple-output (SIMO) radar. Then, one transmitting antenna and multiple receiving antennas are used. The locations of the transmitting and receiving antennas are denoted as $\boldsymbol{L}_T = (X_T, 0)$ and $\boldsymbol{L}_R = (X_R, 0)$, respectively. We assumed an impulse–Doppler radar system. In each observation sequence, a pulse (e.g. Gaussian derivative forms) is repeatedly transmitted from the transmitter with a fixed pulse-repetition interval (PRI) and its time-series response is simultaneously recorded at the receivers. Here, λ is defined as the wavelength corresponding to the centre frequency of a transmitted pulse. The observation model assumes one front wall and two side walls. One rectangular wall is located in front of and parallel to the observation array (referred to as the front wall) and the others are located along the y-axis (referred to as the side wall). Each of the walls comprises low-lossy and homogeneous media with known relative permittivity ε_w and thickness d_w.

For each combination of $\boldsymbol{L}_T$ and $\boldsymbol{L}_R$, the recorded signal is denoted as $s'(\boldsymbol{L}_T, \boldsymbol{L}_R, t, \tau)$, where t denotes a fast time and τ denotes a slow time sampled by the PRI. $s(\boldsymbol{L}_T, \boldsymbol{L}_R, t, \tau)$ is calculated as

$$s(\boldsymbol{L}_T, \boldsymbol{L}_R, t, \tau) = \int_{-\infty}^{\infty} W(\omega) S'(\boldsymbol{L}_T, \boldsymbol{L}_R, \omega, \tau) e^{j\omega t} \, dw, \quad (1)$$

where $S'(\boldsymbol{L}_T, \boldsymbol{L}_R, \omega, \tau)$ is the form of Fourier transform of $s'(\boldsymbol{L}_T, \boldsymbol{L}_R, t, \tau)$ as to t. Note that in a typical radar observation model, the received signal $s(\boldsymbol{L}_T, \boldsymbol{L}_R, t, \tau)$ is expressed as a convolution of the reference signal, $s_{\text{ref}}(t)$ and the object function

(usually expressed as a linear mixture of delta functions) with additive noise $n(t)$. To achieve a higher range resolution in reconstructing the object function (range profile), the filter $W(\omega)$ is introduced as

$$W(\omega) = \frac{S_{\text{ref}}(\omega)^*}{(1 - \eta)S_0^2 + \eta |S_{\text{ref}}(\omega)|^2} S_0, \quad (2)$$

where $\eta = 1/(1 + (S/N)^{-1})$. $S_{\text{ref}}(\omega)$ is the reference signal in the frequency domain, that is, a complex conjugate of the transmitted signal. S_0 is a constant for dimensional consistency. $W(\omega)$ in (2) is the best estimator for the transfer function in a least-square sense in the presence of noise, derived from the Wiener filter [19, 20]. Note that, since we need to deal with multiple reflection signals from multiple objects, it is quite difficult to determine the optimal η; therefore, an appropriate η is determined empirically.

$s(\boldsymbol{L}_T, \boldsymbol{L}_R, t, \tau)$ is converted to $s(\boldsymbol{L}_T, \boldsymbol{L}_R, R', \tau)$, using $R' = ct/2$ with the radio wave speed c. Then, the range–Doppler signals, denoted as $S(\boldsymbol{L}_T, \boldsymbol{L}_R, R', V'_D)$ is obtained through the 1D Fourier transformation of $s(\boldsymbol{L}_T, \boldsymbol{L}_R, R', \tau)$ to τ. The RP is denoted as $\boldsymbol{q} \equiv (\boldsymbol{L}_T, \boldsymbol{L}_R, R, V_d)^T$, which is extracted from the local maxima of $S(\boldsymbol{L}_T, \boldsymbol{L}_R, R', V'_D)$ as shown in

$$\left. \begin{array}{l} \dfrac{\partial^2 S(\boldsymbol{L}_T, \boldsymbol{L}_R, R', V'_D)}{\partial R' \partial V'_D} = 0 \\[2mm] S(\boldsymbol{L}_T, \boldsymbol{L}_R, R', V'_D) \geq \alpha \max_{R', V'_D} S(\boldsymbol{L}_T, \boldsymbol{L}_R, R', V'_D) \\[2mm] V'_D \neq 0, \end{array} \right\} \quad (3)$$

where the threshold parameter $\alpha \geq 0$ is empirically determined. Note that, the second derivative in (3) is processed by a finite differential operation. In addition, since higher-frequency noise components can be suppressed by noise reduction filtering (e.g. matched filtering), the above differential response could be calculated without much divergence, and the extraction of the local maximum offers the desired RP.

Fig. 1*b* shows an example of the range–Doppler signal and the extraction of the RPs, where a one-sided wall and two targets with different velocities are assumed. The RPM-based method assumes that each RP is assigned to a scattering centre on the target boundary, and the conversion of the RPs to the target boundary points is regarded as the imaging process.

3 Original TW-RPM method

This section provides a brief explanation of the original TW-RPM method to aid in understanding the proposed method, which is presented in the following section. Note that the original TW-RPM method only assumed the mono-static observation model. We first describe the methodology of the TW-RPM method using the mono-static model assumption. In this case, the transmitting and
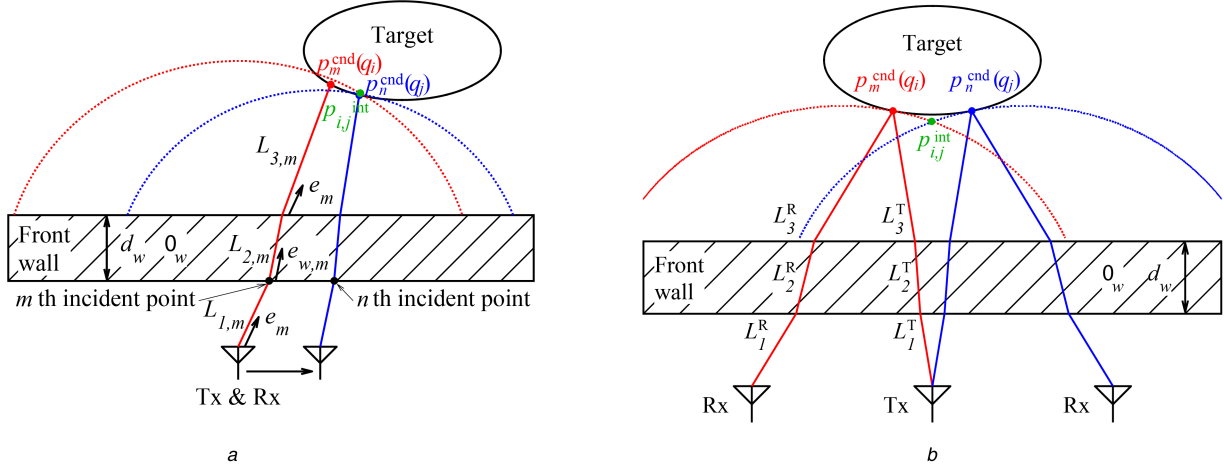
Fig. 2 *Propagation paths (red and blue solid lines) and candidate curves (red and blue broken lines) for scattering centres (red and blue points) on target and its intersection point (green point) in TW-RPM imaging process in*
(a) Mono-static observation, *(b)* Multi-static observation

receiving antennas were located at the same position and were denoted simply as $\boldsymbol{L} = \boldsymbol{L}_T = \boldsymbol{L}_R$. For each extracted RP $\boldsymbol{q}_i \equiv (\boldsymbol{L}_i, \boldsymbol{L}_i, R_i, \tau_i)$, where the subscript i denotes the index number, the propagation path from the antenna to the target through the wall can be derived using Snell's law. Fig. 2a shows the assumed propagation paths from two different locations in the scanning model. Here, we define the candidate curve as the orbit of the end point of the propagation path from the antenna $\boldsymbol{L}$, determined for each range R by the front wall boundary location with thickness d_w and relative permittivity ϵ_w. Although we can directly measure the range R (representing the distance from the antenna to target boundary), the DOA could not be determined using the single antenna observation. Such ambiguity is expressed as a candidate curve, on which the actual scattering centre might exist. The discretised point on the candidate curve (denoted by the broken line in Fig. 2) for the target boundary, $\boldsymbol{p}_m^{\text{cnd}}(\boldsymbol{q}_i)$, is expressed using each incident point (discretely sampled) on the front wall boundary

$$\boldsymbol{p}_m^{\text{cnd}}(\boldsymbol{q}_i) = (L_{1,m} + L_{3,m})\boldsymbol{e}_m + \frac{L_{2,m}}{\sqrt{\epsilon_w}}\boldsymbol{e}_{w,m}, \qquad (4)$$

where m is the discretised index (denoted by natural number) of the incident point of the front–side wall. $L_{1,m}$, $L_{2,m}$ and $L_{3,m}$ denote the propagation lengths as shown in Fig. 2, and $\boldsymbol{e}_m$ and $\boldsymbol{e}_{w,m}$ are denoted as the propagating unit vector outside and inside wall, respectively, which are obtained by d_w and ϵ_w under the Snell's law. Note that, since the scattering-centre point on the target boundary could change with reference to the antenna locations $\boldsymbol{L}_i$ and $\boldsymbol{L}_j$, the candidate curve should be different in terms of $\boldsymbol{q}_i$ and $\boldsymbol{q}_j$ as shown in Fig. 2. Here, the intersection point denoted as point $\boldsymbol{p}_{i,j}^{\text{int}}$ between the two different candidate curves determined by $\boldsymbol{q}_i$ and $\boldsymbol{q}_j$ is approximately calculated using each discretised point on the candidate curve as

$$\boldsymbol{p}_{i,j}^{\text{int}} \equiv \boldsymbol{p}_{\hat{m}}^{\text{cnd}}(\boldsymbol{q}_i), \qquad (5)$$

$$(\hat{m}, \hat{n}) = \arg\min_{(m,n)} \| \boldsymbol{p}_m^{\text{cnd}}(\boldsymbol{q}_i) - \boldsymbol{p}_n^{\text{cnd}}(\boldsymbol{q}_j) \|^2 . \qquad (6)$$

On the basis of the original RPM principle [9], the target point corresponding to the RP $\boldsymbol{q}_i$ is determined as $\hat{\boldsymbol{p}}_i$

$$\hat{\boldsymbol{p}}_i = \arg\max_{\boldsymbol{p}_{i,j}^{\text{int}}} \sum_k s(\boldsymbol{q}_i) \\ \times \exp\left(-\frac{\| \boldsymbol{p}_{i,j}^{\text{int}} - \boldsymbol{p}_{i,k}^{\text{int}} \|^2}{2\sigma_r^2}\right)\exp\left(-\frac{\| \boldsymbol{L}_i - \boldsymbol{L}_k \|^2}{2\sigma_D^2}\right), \qquad (7)$$

where $s(\boldsymbol{q}_i)$ denotes the output quantity of the filter defined in (2) at the RP $\boldsymbol{q}_i$, $\boldsymbol{q}_i \neq \boldsymbol{q}_j$, $\boldsymbol{q}_i \neq \boldsymbol{q}_k$, $\boldsymbol{q}_j \neq \boldsymbol{q}_k$ hold, and σ_r and σ_D are constants, which can be determined by considering the assumed sampling interval of the observation point, detailed in [9]. Equation (7) determines the scattering-centre point corresponding to each $\boldsymbol{q}_i$ among all possible intersection points on the candidate curves, so that the spatial accumulation degree for the intersection points becomes maximised. Note that the term $\exp(-\| \boldsymbol{L}_i - \boldsymbol{L}_k \|^2 / 2\sigma_D^2)$, denotes the weight function, based on the characteristic that the intersection point of $\boldsymbol{p}_{i,j}^{\text{int}}$ should converge to the actual scattering centre when $\boldsymbol{L}_k \to \boldsymbol{L}_i$ as validated in [9]. This method has a distinct advantage over the DAS-based imaging method in that it achieves accurate boundary-shaped reconstruction that considers the scattering-centre shift in relation to the observation point. However, since this method does not consider the double-bounced or higher-order signals, it suffers from a ghost image due to these multiple reflection echoes.

4 Proposed method

To overcome the above-mentioned problem, this paper proposes a multipath exploitation method based on the TW-RPM algorithm with Doppler-based discrimination of double-bounced signals. Since the original TW-RPM method was developed for mono-static observations, this section initially shows an extension to a multi-static observation model, corresponding to the SIMO model. Next, the Doppler-based recognition of double-bounced and direct signals is presented by introducing the prior estimation of target motion and locations with the original TW-RPM algorithm. Finally, the actual application procedure of this method is presented.

4.1 Multi-static extension of TW-RPM

Fig. 2b shows the propagation paths and candidate curves of the multi-static model. Since the transmitting and receiving antennas are located at different positions, the incident and exit points on the front wall boundary are also located in different positions. Then, the discretised points on the candidate curve for the target boundary $\boldsymbol{p}_m^{\text{cnd}}(\boldsymbol{q}_i)$ as shown in Fig. 2b corresponding to an RP $\boldsymbol{q}_i$ is calculated so that it satisfies

$$\left.\begin{aligned} \boldsymbol{p}_m^{\text{cnd}}(\boldsymbol{q}_i) &= (L_{1,m}^T + L_{3,m}^T)\boldsymbol{e}_m^T + \frac{L_{2,m}^T}{\sqrt{\epsilon_w^T}}\boldsymbol{e}_{w,m}^T \\ &= (L_{1,m}^R + L_{3,m}^R)\boldsymbol{e}_m^R + \frac{L_{2,m}^R}{\sqrt{\epsilon_w^R}}\boldsymbol{e}_{w,m}^R, \\ 2R_i &= L_{1,m}^T + L_{2,m}^T + L_{3,m}^T + L_{1,m}^R + L_{2,m}^R + L_{3,m}^R, \end{aligned}\right\} \quad (8)$$

where m is the discretised index (denoted as a natural number) of the front–side wall, and the superscripts 'T' and 'R' denote the transmitting and the receiving antennas, respectively. On the basis of the RPM method, the target point corresponding to q_i is calculated as

$$\hat{p}_i = \arg\max_{p_{i,j}^{\text{int}}} \sum_k s(q_i)$$
$$\times \exp\left(-\frac{\| p_{i,j}^{\text{int}} - p_{i,k}^{\text{int}} \|^2}{2\sigma_r^2}\right) \exp\left(-\frac{D(q_i, q_k)^2}{2\sigma_D^2}\right), \quad (9)$$

instead of (7), where $D(q_i, q_k)$ defines the actual distance between L_T and L_R as

$$D(q_i, q_k) = \min \left(\| L_{T,i} - L_{T,k} \| + \| L_{R,i} - L_{R,k} \|, \right.$$
$$\left. \| L_{T,i} - L_{R,k} \| + \| L_{R,i} - L_{T,k} \| \right). \quad (10)$$

The optimisation problem in (9) is a univariate problem, and hence, it is not very time-consuming even if all the possible intersection points are assessed in maximising the right term of (9) to avoid a local maximum solution.

4.2 Double-bounced signal recognition by Doppler velocity

This section describes the recognition method for double-bounced signal, which enhances the imaging accuracy in applying the above-mentioned multi-static-based TW-RPM method. Here, we introduce Doppler–velocity-based recognition, which can be achieved by an accurate prior estimation of each target motion and location. Note that, while the motion velocity and Doppler velocity are vector variables, the Doppler–velocity vector can be derived from the motion vector's projection on the line of sight (LOS) direction. Thus, even if the motion vector is unchanged, the Doppler–velocity vector can be changed according to the antenna locations, namely different LOS directions. These facts are exploited as a recognition between the single- and double-bounced scattering because these scatterings are considered as single scattering with different transmitting and receiving antenna combination, as in Fig. 3a.

4.2.1 Prior estimation for target motion and location: Initially, this method requires a priori estimation of the propagation path of direct- and double-bounced signals to calculate each Doppler velocity. Fig. 3a shows the propagation paths, which must be considered, as one direct reflection and two double-bounced reflections for each target. Then, to determine each propagation path, the prior estimation of the target motion and the location is required. In actual pulse–Doppler radars, the pulse is sequentially emitted from the transmitter with fixed intervals such as PRI. By focusing on this feature, this method divides these pulse sequences into first and latter half measurements for the above prior estimation. First, two groups of RPs data with non-zero–Doppler

velocities are extracted using the first and latter half of the pulse sequences. The RPs for the first and latter half of the measurement are defined as q_i^F and q_i^L, respectively. Next, each group of RPs is processed by original TW-RPM and the converted target points are defined as p_i^F and p_i^L, respectively. To deal with multiple targets, target points in each observation time are clustered using an appropriate clustering algorithm such as hierarchical clustering algorithm [21]. Next, each target cluster is combined between first and latter halves of the observation based on the proximity of the Doppler velocity. Clustered and combined target points are then redefined as $p_{i,k}^F$ and $p_{i,k}^L$, where superscript $k(=1, 2, \ldots, K)$ denote the corresponding target cluster. The motion vector $v_{\text{init}, k}$ and location $p_{\text{init}, k}$ for the kth target are calculated using the following equations:

$$v_{\text{init}, k} = \frac{2}{T_c}\left(\sum_{i=1}^{N_k^L} \frac{p_{i,k}^L}{N_k^L} - \sum_{i=1}^{N_k^F} \frac{p_{i,k}^F}{N_k^F}\right), \quad (11)$$

$$p_{\text{init}, k} = \frac{1}{2}\left(\sum_{i=1}^{N_k^L} \frac{p_{i,k}^L}{N_k^L} + \sum_{i=1}^{N_k^F} \frac{p_{i,k}^F}{N_k^F}\right), \quad (12)$$

where T_c denotes the observation time and N_k^L and N_k^F are the quantities of $p_{i,k}^L$ and $p_{i,k}^F$, respectively.

4.2.2 RPs clustering using Doppler velocities: If the front- and side-wall locations are given, the actual Doppler velocities and time delays of double-bounced reflections can be determined by prior estimation of target motion and location determined with the ray-tracing approach. In particular, since we assume the gravity points of the RPM target points, the single- and double-bounced paths and their time delays can be determined by the ray-tracing method using the relative permittivity and thickness of the wall as shown in Fig. 3a. In addition, the associated Doppler velocity is determined sequentially by the difference in time delays. Thereafter, that, by associating the observed (measured RPs q_i) and calculated (estimated from a priori estimation using RPM images) Doppler velocities and ranges in the range–Doppler space, each RP q_i can be associated with an appropriate path such as S-k, D1-k or D2-k, where S-k, D1-k and D2-k denote the calculated propagation paths of one direct- and two double-bounced reflections, respectively, determined by $v_{\text{init}, k}$ and $p_{\text{init}, k}$. Fig. 3b shows an example of the observed and the calculated RPs association in a range–Doppler space. As shown in Fig. 3a, the Doppler–velocity vector for the single- and double-bounced signals could be different because of their different paths, even if the target motion vector remains unchanged. Thus, we can discriminate single- and double-bounced signals on the range–Doppler maps as shown in Fig. 3b, using the prior estimation of the target motion and location vector. Finally, each RP should be processed by the TW-RPM
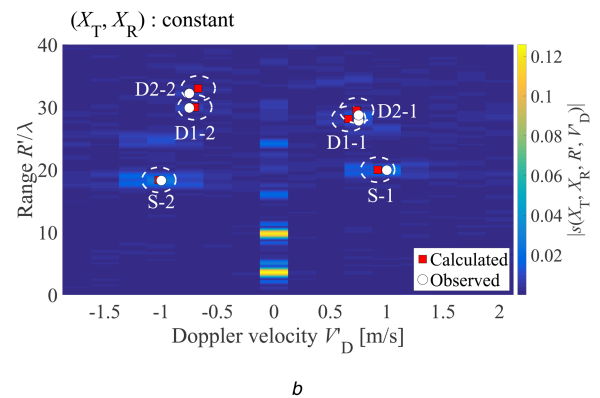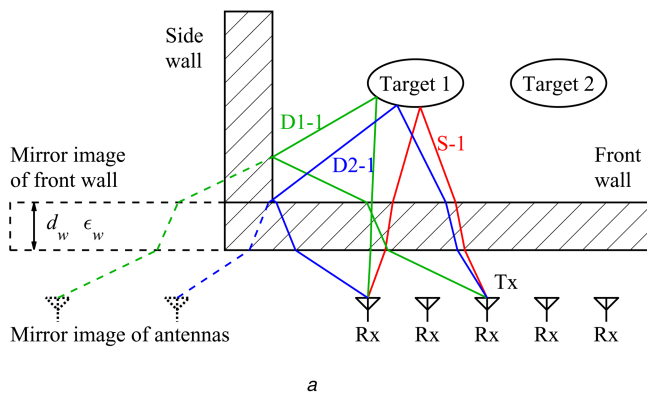
Fig. 3 *Double-bounced signal recognition by Doppler velocity*
(a) Direct- and two double-bounced reflection paths in the bi-static configuration and equivalent antenna locations mirrored by the side wall. (D1-2 and D2-2 are omitted.), *(b)* Example of RPs clustering on range–Doppler data, where the red squares are denoted as calculated range–Doppler set and the white circles are denoted as observed one

method, where the equivalent antenna location is the mirror location of an actual one in the case of a double-bounced cluster. Note that, the equivalent aperture size is enhanced by correctly employing double-bounced signals, which is one advantage of the proposed method.

4.3 Procedure for the proposed method

The actual procedure for the proposed method is as follows:

Step (1): Signals are recorded at each slow time τ (PRI snapshot) as $s(\boldsymbol{L}_T, \boldsymbol{L}_R, t, \tau)$ and are processed by the filter defined in (2), denoted as $s(\boldsymbol{L}_T, \boldsymbol{L}_R, R', \tau)$.

Step (2): Range–Doppler data corresponding to the first and latter halves of pulse hits are obtained by applying the 1D Fourier transform along the slow time direction with a limited time window, where the zero–Doppler components are eliminated. Here, the range–Doppler data for the first and latter halves of the pulse hits are denoted as $S^F(\boldsymbol{L}_T, \boldsymbol{L}_R, R', V'_D)$ and $S^L(\boldsymbol{L}_T, \boldsymbol{L}_R, R', V'_D)$, respectively.

Step (3): RPs for the first and latter halves of the pulse hits are extracted as $\boldsymbol{q}_i^F$ and $\boldsymbol{q}_i^L$, respectively, from the local maximum of each range–Doppler data as in (3).

Step (4): Each set of RP for $\boldsymbol{q}_i^F$ and $\boldsymbol{q}_i^L$ are processed by the multi-static TW-RPM method as in (9), and each target point $\boldsymbol{p}_i^F$ and $\boldsymbol{p}_i^L$ clustered to the kth target, as $\boldsymbol{p}_{i,k}^F$ and $\boldsymbol{p}_{i,k}^L$, respectively.

Step (5): Initial velocity vector $\boldsymbol{v}_{\text{init}, k}$ and location $\boldsymbol{p}_{\text{init}, k}$ for the kth target cluster are calculated as in (11) and (12).

Step (6): Range–Doppler data corresponding to all the pulse hits are obtained by applying the 1D Fourier transform, and RPs extracted as $\boldsymbol{q}_i$ using (3).

Step (7): Each RP $\boldsymbol{q}_i$ is associated with appropriate paths S-k, D1-k or D2-k by searching the minimal proximity between the observed RP ($\boldsymbol{q}_i$) and the calculated (estimated) RP on the range–Doppler map as shown in Fig. 3b.

Step (8): For all RPs in each cluster, the multi-static TW-RPM method is applied by considering the single- and double-scattering paths, namely the transmitting and receiving antenna locations as shown in Fig. 3a.

5 Evaluation in numerical simulation

This section shows the performance evaluation conducted with FDTD-based numerical simulation. The transmitting current forms the pulse modulated signal, where the centre frequency is 6 GHz and the effective bandwidth is 2 GHz corresponding to its theoretical range resolution in the air of 75 mm. The centre wavelength is $\lambda = 50$ mm. Note that the reason for assuming a 6 GHz band pulse is that there is a legal regulation regarding the UWB spectrum mask determined by the federal communication committee [22], other institutions or governments. In this regulation, the frequency band from 1 to 3 GHz is strictly limited to lower emission levels compared with the emission levels of higher-frequency bands. In addition, the wall attenuation impact is proportional to the square root of frequency, and the 6 GHz radar band does not have so much negative impact on signal loss, compared with lower radar bands. The 21 receiving antennas are linearly arranged at an equal spacing of 1.0λ in the range $-10.0\lambda < x < 10.0\lambda$. The transmitting antenna is set on the origin point. The front wall is set parallel to the array antennas, and the distance between them is set as 2.0λ. The thickness, relative permittivity, and conductivity of the front and side walls are set at $d_w = 2.0\lambda$, $\varepsilon_w = 10.0$ and $\sigma_w = 0.005$ S/m and are given for any imaging process. The side wall is set vertical to the front wall as shown in Fig. 1. Two ellipsoid targets with 50 relative permittivities and 1.0 S/m conductivity modelling human body are set behind the front wall, and the major axis and minor axes of all targets are set at $a = 6.0\lambda$ and $b = 3.0\lambda$, respectively. Here, #1 and #2 targets have the constant velocity vectors as $\boldsymbol{v}_1 = (0, 20\lambda)[1/s]$ and $\boldsymbol{v}_2 = (0, -20\lambda)[1/s]$, respectively, and the centre positions of

the movements of #1 and #2 targets are set as $(-5.0\lambda, 15\lambda)$ and $(5.0\lambda, 15\lambda)$. No clutter object is assumed here, except for walls. The observation time is set as $T_c = 0.1$s, and the number of receptions is 16. The Doppler–velocity resolution is 0.25 m/s. We assume that the velocity of an object is invariant in the observation time (T_c), and this assumption is not impractical as to human motion. Subsequently, $S/N = 8$ dB is defined as the ratio of the peak power of the signal to the average noise power of $s'(\boldsymbol{L}_T, \boldsymbol{L}_R, t, \tau)$ in the time (t) domain. Therefore, S/N is calculated for the raw data before converting the result to the range–Doppler map. Here, to make it a clear side-wall effect, we test the two cases below as a single-side wall (Case 1) and a double-side wall (Case 2), with each dielectric constant, thickness and location given in the simulation.

5.1 Single-side-wall cases (case 1)

We test the single-side-wall as follows. Fig. 4a shows the image generated by the DAS approach without considering the double-scattering paths, as a method of comparison. This figure shows that while the strong responses around the actual target boundary, these images are not sufficiently accurate for boundary estimation, and non-negligible responses from double-bounced reflections are focused behind the actual target, regarded as a ghost image. Fig. 4b shows the target boundary points estimated by the original multi-static TW-RPM method, where double-bounced recognition is not considered. Here, $\alpha = 0.1$, $\sigma_r = 0.02\lambda$ and $\sigma_D = 0.5\lambda$ are set, the selection criteria of which are detailed in [9]. This result demonstrates that the estimated points accurately reconstruct the front side of target boundaries. Although it is difficult to compare the images by DAS and TW-RPM in fair criteria, these results qualitatively indicate that TW-RPM method offers more accurate boundary estimation compared with DAS approach. However, there are so many reconstructed points (ghost images) behind the actual targets resulting from the double-bounced reflections in both TW-RPM and DAS approaches. Note that, there are strong responses along the backside of the front wall boundary in both Figs. 4a and c. It is believed that these responses are caused by the reflection from the front and side walls, and their multiple reflections within the wall media. In particular, there are strong responses along the intersection of the front- and left-side walls in Fig. 4c (the area $-13\lambda \leq x \leq -5\lambda$ and $4\lambda \leq y \leq 6\lambda$). It is also believed that the multiple reflections from the walls are positively interfered along the above area, by the DAS process considering the double-scattering paths.

Next, Fig. 4c shows the image generated by DAS approach which considers double-bounced reflection, which is referred from [13]. Although ghost images are suppressed by consideration of double-bounced reflection paths, the reconstructed boundary does not express the actual one, and the grating lobe responses also cause periodical pattern on the actual boundary. Finally, we demonstrate the result of the proposed method as follows. Fig. 5a shows the output of the filter defined in (2) at the certain snapshot of pulse-repetition sequences, and extracted RPs associated with its propagation path types (red: S, yellow: D1 and blue: D2). Here, the observed RPs are associated with their propagation paths (S, D1 and D2) for each clustered target by the proposed method, with the threshold parameters $\alpha = 0.2$. Note that, the strong reflections from the front wall can be ignored by eliminating zero–Doppler–velocity components. Fig. 5b shows the reconstruction results by the proposed method and demonstrates that the ghost images behind the targets that appeared in the original method are remarkably suppressed. In addition, the RPs ascribed from double-bounced reflections are accurately located around the actual boundary. However, there are some estimated target points that deviated significantly from the actual boundary. This is because the interference among these signals produces an inappropriate association between the RP and the propagation path.

For quantitative evaluation, the reconstruction error $e(\boldsymbol{p}_i^{\text{est}})$ is calculated as

$$e(\boldsymbol{p}_i^{\text{est}}) = \min_{\boldsymbol{p}^{\text{true}}} \| \boldsymbol{p}_i^{\text{est}} - \boldsymbol{p}^{\text{true}} \|_2 , \quad (i = 1, 2, \ldots, N_{\text{T}}), \quad (13)$$

where $\boldsymbol{p}_i^{\text{est}}$ and $\boldsymbol{p}^{\text{true}}$ are the locations of the ith estimated point and the true target point (discrete points on target boundaries obtained with sufficiently dense sample size), respectively, and N_{T} is the total number of $\boldsymbol{p}_i^{\text{est}}$. Fig. 5c shows the cumulative distribution for $\boldsymbol{p}_i^{\text{est}}$ without double-bounced recognition (the original TW-RPM method) and with the recognition (the proposed TW-RPM method). The numbers of estimated points and the cumulative probabilities satisfying $e(\boldsymbol{p}_i^{\text{est}}) < 1.0\lambda$ for the original and proposed methods, are 164 points and 103 points, 26.8 and 93.2%, respectively. This quantitative evaluation demonstrates the effectiveness of the proposed method in terms of reconstruction accuracy.

5.2 Double-side-wall case (case 2)

The case of the double-side wall is investigated as follows. Fig. 6a shows the imaging result of the DAS approach without considering the double-bounced paths and Fig. 6b indicates that obtained by the original multi-static TW-RPM method. As in Case 1, the original TW-RPM method accurately reconstructs the target boundary while the DAS approach suffers from a blurred image around the boundary. Also, the ghost images behind the targets, especially in Fig. 6b are severely enhanced compared with Case 1, due to more double-bounced reflections from double-side walls.

On the contrary, Fig. 6c shows the imaging result of DAS which considers double-bounced reflection and denotes that its ghost images behind the targets are considerably suppressed. However, the estimated target boundary is not clear and accuracy is insufficient, and there are interference fringes caused by grating lobe effect, where some intervals of virtual arrays are over a half of

wavelength. Next, we show the result of the proposed multi-static TW-RP. At first, Fig. 7a shows the output of the filter defined in (2), with the extracted RPs associated with its propagation path types (red: S, yellow: D1 and blue: D2). Noted that the number of processed RPs is considerably increased and the determination of the association with the appropriate propagation path becomes more difficult. Fig. 7b shows the target boundary points estimated by the proposed TW-RPM and demonstrates that the proposed method perfectly suppresses the ghost images and accurately reconstructs the actual target boundary, even in such complicated situation.

Finally, Fig. 7c shows the cumulative distribution for $\boldsymbol{p}_i^{\text{est}}$ in Case 2. In the original and proposed RPM-based methods, the numbers of estimated points and the cumulative probabilities satisfying $e(\boldsymbol{p}_i^{\text{est}}) < 1.0\lambda$ are 238 points and 172 points, 19.3 and 97.1%, respectively. This quantitative evaluation shows the effectiveness of the proposed method in terms of accuracy for an increased number of side walls.

5.3 Sensitivity to wall parameter errors

In actual scenario, one must consider the estimation errors of parameters such as relative permittivity and thickness of the wall. This section investigates the sensitivity test of the proposed method to the wall parameters as ϵ_{w} and d_{w}. Fig. 8 shows the imaging results obtained by the proposed method, where ϵ_{w} and d_{w} have 10% errors from the actual set ($\epsilon_{\text{w}} = 10.0$ and $d_{\text{w}} = 10.0\,\text{cm}$). As shown in Fig. 8, there are non-negligible errors, especially for the overestimation case for ϵ_{w} and d_{w}, which is caused by offset errors in estimating actual distance to the target. However, a relative error within a group of target points are not so much deviated, and any image offers a part of the original ellipsoid shape, which could not
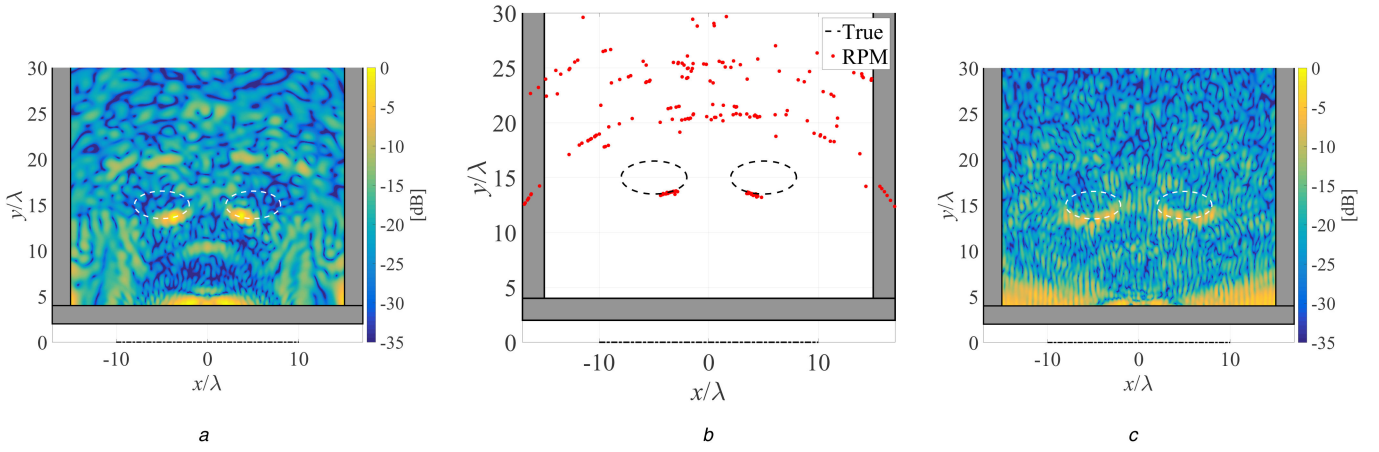

a   b   c
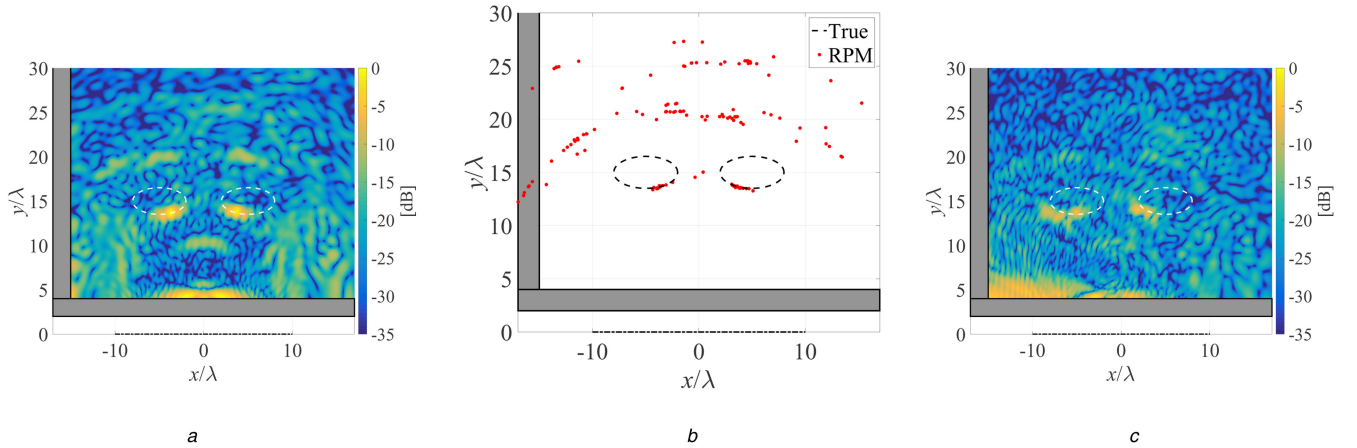
Fig. 4 *Single-side-wall cases (case 1)*
(a) Reconstructed image by DAS method at Case 1 without consideration of double-bounced signal paths, *(b)* Reconstructed target boundary points by the original multi-static TW-RPM at Case 1, *(c)* Reconstructed image by DAS method at Case 1 with consideration of double-bounced signal paths
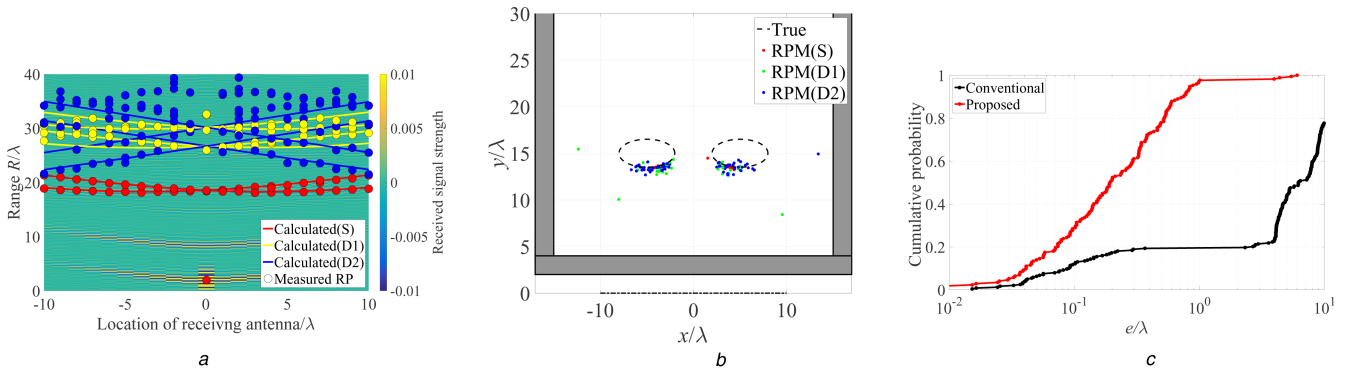

a   b   c
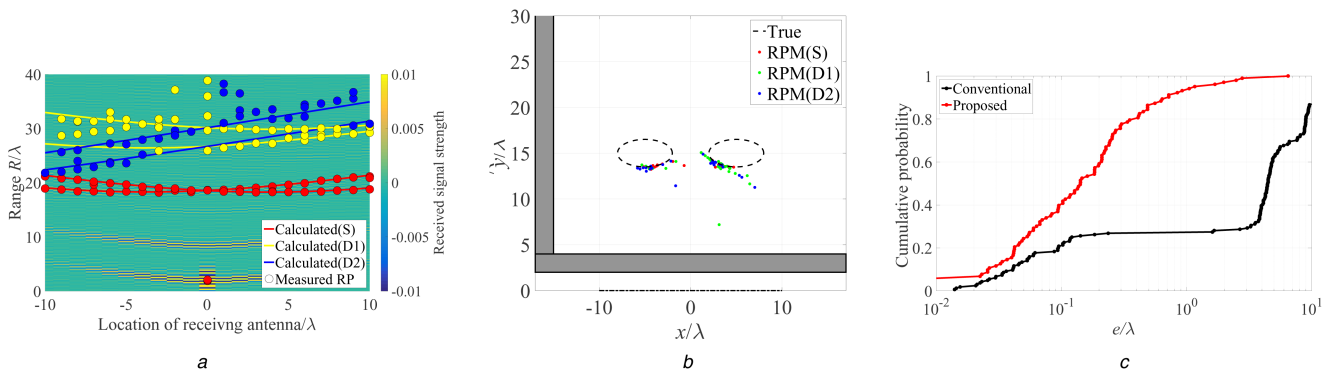
Fig. 5 *Output of the filter*
(a) RP distribution associated with its propagation path types (red: S, yellow: D1 and blue: D2), where each curve denotes the calculated path from prior estimation of target motion and location at Case 1, *(b)* Reconstructed target boundary points by the proposed method at Case 1, *(c)* Cumulative distribution for reconstruction errors for the original and proposed TW-RPM methods at Case 1

Fig. 6 *Double-side-wall case (case 2)*
(a) Reconstructed image by DAS method at Case 2 without consideration of double-bounced signal paths, *(b)* Reconstructed target boundary points by the original multi-static TW-RPM at Case 2, *(c)* Reconstructed image by DAS method at Case 2 with consideration of double-bounced signal paths

Fig. 7 *Output of the filter*
(a) RP distribution associated with its propagation path types (red: S, yellow: D1 and blue: D2), where each curve denotes the calculated path from prior estimation of target motion and location at Case 2, *(b)* Reconstructed target boundary points by the proposed method at Case 2, *(c)* Cumulative distribution for reconstruction errors for the original and proposed TW-RPM method at Case 2
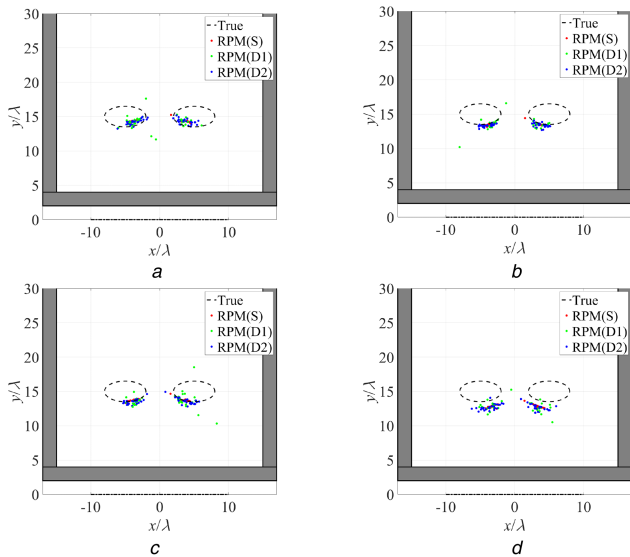
Fig. 8 *Reconstructed target boundary points by the proposed method, where ϵ_w and d_w have errors from the actual one*
(a) Case in $\epsilon_w = 9.0$ and $d_w = 9.0$ cm, *(b)* Case in $\epsilon_w = 9.0$ and $d_w = 11.0$ cm, *(c)* Case in $\epsilon_w = 11.0$ and $d_w = 9.0$ cm, *(d)* Case in $\epsilon_w = 11.0$ and $d_w = 11.0$ cm

be obtained by DAS-based image. Note that if we know the dielectric constant of the wall, the above problem would be eliminated using other permittivity estimation methods such as ellipsometry [23] or inverse scattering analysis, and we will incorporate imaging and permittivity estimation in our future endeavour. Furthermore, this simulation model assumes homogeneity of the wall; it is easy to predict that the imaging accuracy of the RPM or other DAS-based methods degrade for the heterogeneous walls. However, the literature in [24] have already demonstrated that the original RPM offered robust images in heterogeneous surrounding media but the application range of these methods to be investigated further in future work.

6 Conclusion

This research proposed a novel TW imaging approach based on the RPM method and Doppler-based signal recognition for direct- and double-bounced signals. The proposed method uses an initial estimate of each target's location and motion for each target clustered using the original RPM method, which enabled us to estimate the Doppler velocity and range derived from direct paths and two types of double-bounced paths. The FDTD-based analysis assumed a 6 GHz centre for the UWB TW-radar scenario, and this demonstrated that the proposed method successfully suppressed ghost images by recognising the double-bounced signals without prior knowledge of each target shape, location and motion in single-side-wall and double-side-wall cases. The imaging accuracy of the proposed method naturally depends on the accuracy and resolution of the range–Doppler data. Note that, as to a static object, it is possible to offer an image by using a zero–Doppler component, while we need to consider the interference from wall reflection. In the case of a relatively wider fractional band, which was assumed in this case, Fourier-transformation-based range–Doppler extraction was not suitable because the signal pulse would move over the range resolution in the measurement interval. With further research, we hope to introduce an even more suitable approach such as a kernel-based approach [25]. Note that though the S/N level assumed in the simulation in Sections 5.1 and 5.2 are not much higher, the filtering process using (2) and the coherent

integration along the slow time direction considerably enhance the equivalent *S/N* leading to the noise-robustness of the proposed method. However, in realistic scenarios, the effects of other clutters (*e.g.* furniture) that were not considered in this simulation need to be considered. Since most clutters are static, the zero–Doppler elimination considerably suppresses the static clutter responses. Nevertheless, the multiple reflections between the target and clutter (except for the wall) could interfere with the target responses that have non-zero–Doppler components. In such cases, the accuracy of the Doppler discrimination or the RPM imaging performance is expected to degrade. Furthermore, in 3D problems, we must consider the multiple-scattering effects from the ceiling or the floor that make the problem more complicated. Thus, it is our important work in the future to test the experimental data analysis of the proposed method under realistic scenarios.

7 Acknowledgment

8 References

[1] Wang, G., Amin, M.G.: 'Imaging through unknown walls using different standoff distances', *IEEE Trans. Signal Process.*, 2006, **54**, (10), pp. 4015–4025

[2] Dubroca, R., Fortino, N., Dauvignac, J.-Y.*, et al.*: 'Time reversal-based processing for human targets detection in realistic through-the-wall scenarios'. European Radar Conf. (EuRAD), Manchester, UK, 2011

[3] Li, J., Cai, H., Chen, J.*, et al.*: 'Datum correction based on wave equation inversion in time for UWB through-the-wall radar', *IET Radar Sonar Navig.*, 2017, **11**, (7), pp. 1116–1123

[4] Dang, V., Kilic, O.: 'Simulation framework for compressive sensing-based through-wall detection of moving targets', *IET Radar Sonar Navig.*, 2017, **11**, (9), pp. 1349–1358

[5] Chen, X., Chen, W.: 'Multipath ghost elimination for through-wall radar imaging', *IET Radar Sonar Navig.*, 2016, **10**, (2), pp. 299–310

[6] Guo, S., Cui, G., Wang, M.*, et al.*: 'Similarity-based multipath suppression algorithm for through-wall imaging radar', *IET Radar Sonar Navig.*, 2017, **11**, (7), pp. 1041–1050

[7] Setlur, P., Alli, G., Nuzzo, L.: 'Multipath exploitation in through-wall radar imaging via point spread functions', *IEEE Trans. Image Process.*, 2013, **22**, (12), pp. 4571–4586

[8] Leigsnering, M., Ahmad, F., Amin, M.G.*, et al.*: 'Parametric dictionary learning for sparsity-based TWRI in multipath environments', *IEEE Trans. Aerosp. Electron. Syst.*, 2016, **52**, (2), pp. 532–547

[9] Kidera, S., Sakamoto, T., Sato, T.: 'Accurate UWB radar three-dimensional imaging algorithm for a complex boundary without range point connections', *IEEE Trans. Geosci. Remote Sens.*, 2010, **48**, (4), pp. 1993–2004

[10] Fayazi, S.S., Yang, J., Lui, H-S.: 'UWB SAR imaging of near-field object for industrial process applications'. European Conf. Antennas Propagation (EuCAP), Gothenburg, Sweden, 2013

[11] Salman, R., Willms, I.: '3D UWB radar super-resolution imaging for complex objects with discontinuous wavefronts'. IEEE Int. Conf. Ultra-Wideband (ICUWB), Bologna, Italy, 2011

[12] Kidera, S., Gao, C., Taniguchi, T.*, et al.*: 'Ellipse based image extrapolation method with RPM imaging for through-the-wall UWB radar'. IEEE Int. Geoscience and Remote Sensing Symp. (IGARSS), Milan, Italy, 2015

[13] Setlur, P., Amin, M.G., Ahmad, F.: 'Multipath model and exploitation in through-the-wall and urban radar sensing', *IEEE Trans. Geosci. Remote Sens.*, 2011, **49**, (10), pp. 4021–4034

[14] Leigsnering, M., Amin, M.G., Ahmad, F.*, et al.*: 'Compressive sensing-based multipath exploitation for stationary and moving indoor target localization', *IEEE J. Sel. Top. Signal Process*, 2015, **9**, (8), pp. 1469–1483

[15] Liu, J., Cui, G., Jia, Y.: 'Sidewall detection using multipath in through-wall radar moving target tracking', *IEEE Geosci. Remote Sens. Lett.*, 2015, **12**, (6), pp. 1372–1376

[16] Gennarelli, G., Soldovieri, F.: 'Radar imaging through cinderblock walls: achievable performance by a model-corrected linear inverse scattering approach', *IEEE Trans. Geosci. Remote Sens.*, 2014, **52**, (10), pp. 3749–6738

[17] Kidera, S., Sakamoto, T., Sato, T.: 'Extended imaging algorithm based on aperture synthesis with double-scattered waves for UWB radars', *IEEE Trans. Geosci. Remote Sens.*, 2011, **49**, (12), pp. 5128–5139

[18] Kidera, S., Kirimoto, T.: 'Fast and shadow region 3-dimensional imaging algorithm with range derivative of doubly scattered signals for UWB radars', *IEEE Trans. Antennas Propag.*, 2012, **60**, (2), pp. 984–996

[19] Kessel, R.: 'Wiener filter estimation of transfer functions', *J. Exp. Anal. Behav.*, 2004, **81**, (3), pp. 289–296

[20] Gonzalez, R.C., Wintz, P.A.: '*Digital image processing reading*' (Addison-Wesley Publishing, MA, 1987, 2nd edn.)

[21] Yamaguchi, R., Kidera, S., Kirimoto, T.: 'Accurate imaging method for moving target with arbitrary shape for multi-static UWB radar', *IEICE Trans. Commun.*, 2013, **E96-B**, (7), pp. 2014–2023

[22] Aiello, R., Batra, A.: '*Ultra wideband systems, technologies and applications*' (Newnes Publication, Oxford, Boston, 2006), pp. 17–52

[23] Friederich, B., Schultze, T., Willms, I.: 'UWB-radar based surface permittivity estimation in hostile and pathless security scenarios'. Proc. IEEE ICUWB 2014, Paris, France, 1–3 September 2014, pp. 125–128

[24] Akune, K., Kidera, S., Kirimoto, T.: 'Accurate and nonparametric imaging algorithm for targets buried in dielectric medium for UWB radars', *IEICE Trans. Electron.*, 2012, **E95-C**, (8), pp. 1389–1398

[25] Setsu, M., Kidera, S.: 'Super-resolution Doppler velocity estimation by Gaussian-kernel based range–Doppler conversion for UWB radar'. Progress in Electromagnetics Research Symp., Singapore, Singapore, 2017, pp. 1306–1311